

Crystal growth in nano-confinement: Subcritical cavity formation and viscosity effects

Luca Gagliardi and Olivier Pierre-Louis

CNRS, ILM Institut Lumière Matière,
Université Claude Bernard Lyon 1 Campus LyonTech-La Doua Batiment
Brillouin, 10 rue Ada Byron F-69622 Villeurbanne, France

E-mail: luca.gagliardi@univ-lyon1.fr, olivier.pierre-louis@univ-lyon1.fr

Abstract. We report on the modeling of the formation of a cavity at the surface of crystals confined by a flat wall during growth in solution. Using a continuum thin film model, we discuss two phenomena that could be observed when decreasing the thickness of the liquid film between the crystal and the wall down to the nanoscale. First, in the presence of an attractive Van Der Waals contribution to the disjoining pressure, the formation of the cavity becomes sub-critical, i.e., discontinuous. In addition, there is a minimum supersaturation required to form a cavity. Second, when the thickness of the liquid film between the crystal and the substrate reaches the nanoscale, viscosity becomes relevant and hinders the formation of the cavity. We demonstrate that there is a critical value of the viscosity above which no cavity will form. The critical viscosity increases as the square of the thickness of the liquid film. A quantitative discussion of model materials such as Calcite, Sodium Chlorate, Glucose and Sucrose is provided.

Keywords: Crystal growth, Nano-confinement, Pattern formation, Interfacial phenomena, Thin fluid film, Geophysics

1. Introduction

Crystal growth is commonly confined in pores, faults, or gaps, as observed for example in rocks, in natural and artificial cements, or in biomineralization. In these conditions, crystals can be directly formed on substrate surfaces —such as during heterogeneous nucleation [1, 2, 3, 4, 5], or can be sedimented on substrates due to gravity. The subsequent growth then occurs in the presence of a contact with a substrate. Here, we wish to discuss the growth dynamics with the simplest type of contact, i.e. with a flat, rigid, and impermeable wall.

While growth can then occur at the free surface away from the contacts via bulk transport of growth units, growth in the contact regions requires mass transport along the interface between the crystal and the substrate [6] when the substrate is impermeable. The presence of a liquid film in the contact is therefore a key ingredient to allow for such mass transport along the interface during solution growth, as discussed in the literature [7, 8, 9].

A recent combination of experiments with optical measurements and modeling via a thin film model has shown that when mass supply through the liquid film is insufficient, growth cannot be maintained in the central part of the contact, and a cavity forms in the crystal within the contact region [9]. In later stages, the cavity expands and gives rise to a rim along the edge of the contact. Such rims have been observed in many previous experiments [10, 11, 12, 13] focusing on the crystallization force produced by the growth process [14, 15, 8, 16], which is known to have important consequences for deformation and fracturing of rocks, and the weathering of building materials [17, 18]. However, here we wish to focus on the case where external forces are small, which correspond for example to the experiments of Ref.[9], where the crystal was only weakly maintained against the substrate due to its own weight.

These experiments were also realized with liquid film thicknesses in the range from 10 to 100nm due to the presence of nano-scale roughness or dust between the crystal and the substrate. Our aim here is to investigate the possible changes in this scenario when the thickness of the film is decreased down to the nanometer scale using a thin film model [19, 9] which accounts consistently for thermodynamics, non-equilibrium transport processes (diffusion and advection) and crystal-surface interaction.

At the nanoscale, novel ingredients come into play. The first type of ingredient is related to disjoining pressure effects, which describe the energetic cost of placing the crystal surface at a given distance from the substrate.

The standard theory of disjoining pressure, named the DLVO approach [20], combines two effects. The first one is an electrostatic double-layer repulsion due to the redistribution of charged ions close to the surfaces. These forces are exponentially decreasing with the distance. They are repulsive between similar surfaces but can be both repulsive or attractive between dissimilar surfaces [20, 21]. The second contribution to the DLVO theory are Van der Waals forces, which lead to longer-range power-law interactions between surfaces. Van der Waals interactions are usually attractive for a liquid film between two solid surfaces [20, 21]. In the past decades, significant deviation from the DLVO theory were measured at short ranges (few nanometers). These additional (usually repulsive) interactions related, e.g., to the local ordering or binding of water molecules, are referred to as hydration forces [22, 23, 24, 25]. The sum of long range attractive forces and of short-range repulsive forces gives rise to a minimum in the interaction potential, which corresponds to an equilibrium thickness for the liquid film, hereafter denoted as h . This distance

is usually in the scale from 1 to 10 nm [20]. In the presence of such a minimum, heterogeneous nucleation can occur on the substrate, because there is a gain of energy in growing with an interface in this minimum. Hence, our study could describe growth along a flat substrate after heterogeneous nucleation.

In order to account for these effects in our model, we use a disjoining pressure with an attractive Van Der Waals contribution together with a generic effective short range repulsion. We show that the presence of an attraction makes the appearance of the cavity discontinuous. Indeed, various quantities, such as the depth of the cavity, exhibit a jump at the transition. In addition, there is a minimum supersaturation needed to induce cavity formation. However, the non-equilibrium morphology diagram describing the occurrence of the cavity remains unaffected as compared to the case where disjoining pressure is purely repulsive.

As a second ingredient which becomes relevant when the film thickness is decreased down to the nanoscale is viscosity. Indeed we observe that viscosity hinders the formation of the cavity. We also show the existence of a critical viscosity above which cavities cannot form. We determine the value of the critical viscosity and find it to be proportional to the square of the film thickness. This result can also be reformulated as the existence of a critical thickness below which the cavity will not form for a given viscosity.

We accompany the presentation of model results with a semi-quantitative discussion of the nano-confined growth of some materials, viz., Calcium Carbonate, Sodium Chlorate, Glucose and Sucrose. Although they belong to disparate classes of materials, with time-scales ranging from second to geological times and contact lengthscales from microns to centimeters, our modeling approach suggests that their behavior can be globally classified based on a small number of dimensionless physical parameters.

2. Model and methods

We consider a system with a confinement geometry similar to that of the experiments in [9]: a growing crystal is separated from a flat, impermeable and inert substrate by a thin film of solution. However, here, the film thickness is assumed to be of the order of nanometers. We assume the presence of a macroscopic concentration reservoir outside the contact region.

To predict the evolution of the confined interface during crystal growth, we use the thin film model presented in [19]. This model describes the growth of a rigid crystal, and accounts for diffusion and hydrodynamics in the liquid film. We assume that the slope of the crystal surface is small. Dynamical equations for the interface evolution can therefore be obtained by means of the standard lubrication expansion [26]. Within this limit, due to the slenderness of the film, attachment-detachment kinetics is fast as compared to diffusion along the liquid film. This assumption is more robust when considering highly soluble materials. In addition, we neglect hydrodynamic flow induced by crystal-solution density difference, assume the dilute limit and linearized Gibbs-Thomson relation. We also assume for simplicity an axisymmetric geometry.

The system can be visualized in figure 1, where the profile of the crystal projected along the radius, represented in white, is growing via transport of mass from the macroscopic solution reservoir at the boundary of the simulation box to the crystal surface via the thin film solution. The velocity field of the liquid is represented by the

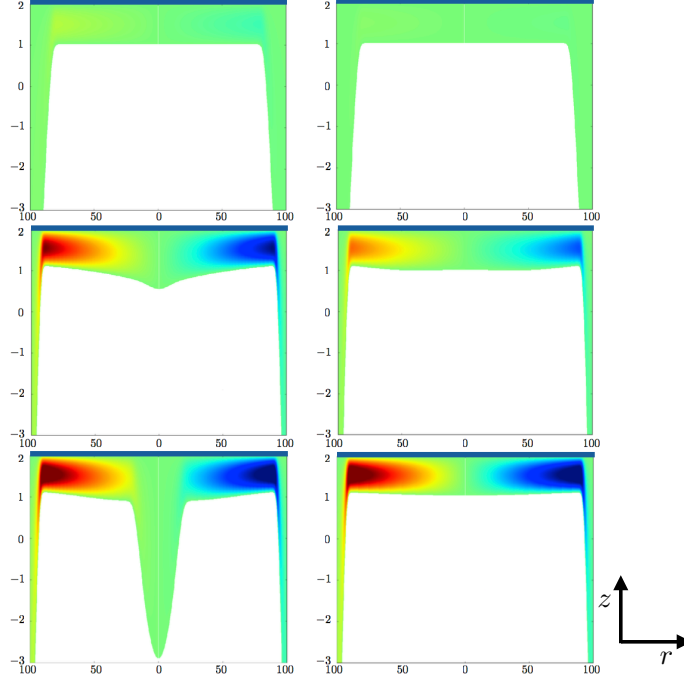


Figure 1. Simulation screenshots representing section of an axisymmetric growing crystal (white). Time flows from top to bottom. The normalized supersaturation is for both panels $\bar{\sigma}_{bc} = 0.21$. Left column $\bar{\eta} = 10^{-2}$; right column $\bar{\eta} = 10^{-1}$, the cavity is not observed. The units of the vertical scale is 1 nm. The substrate is located at $h_s = 2\text{nm}$. The scale of the horizontal axis depends on the material. For instance for NaClO_3 the radial scale unit is 3.2nm. The color-map represents the liquid velocity in normalized units. Red color: positive velocities (flow from left to right); blue: negative velocities; green: vanishing velocity. The physical liquid velocity depends on the material, for instance in the left panel for NaClO_3 its maximum value (darker color) is $u_L \approx 66\mu\text{m/s}$.

color map and the substrate is represented by the dark-blue rectangle at the top of the images.

Let us now describe the evolution equations in more details. Using cylindrical coordinates z, r , mass conservation leads to a dynamical equation relating the local film thickness $\zeta(r, t)$, and the vertical rigid-body translational velocity of the crystal u_z along z

$$\partial_t \zeta = -B \frac{1}{r} \partial_r \left[r \zeta \partial_r (\Delta\mu/\Omega) \right] - u_z, \quad (1)$$

$$\Delta\mu/\Omega = \tilde{\gamma} \partial_{rr} \zeta + \frac{\tilde{\gamma}}{r} \partial_r \zeta - U'(\zeta), \quad (2)$$

where $B = D\Omega^2 c_0 / (k_B T)$ is an effective mobility, with D the diffusion constant, Ω the molecular volume, c_0 the numerical solubility, k_B the Boltzmann constant and T the temperature. In the local chemical potential $\Delta\mu$, the first two terms represent the contribution of surface tension $\gamma(\theta)$ ($\theta = 0$ surface parallel to substrate). These terms are proportional to the surface stiffness $\tilde{\gamma} = \gamma(0) + \gamma''(0)$. The last term represents the contribution of the interaction potential $U(\zeta)$ between the substrate and the crystal.

Since we here focus on small distances ζ , we need to account for the Van Der Waals contribution to $U(\zeta)$, which is usually attractive for a liquid film between two solids [20]. We also included a short range repulsive term to account for a generic effective repulsion preventing contact. The interaction potential then reads

$$U(\zeta) = \frac{A}{12\pi} \left(-\frac{1}{\zeta^2} + \frac{2h}{3\zeta^3} \right), \quad (3)$$

where A is the Hamaker constant and h the equilibrium thickness. It follows that the term appearing in (2) is

$$U'(\zeta) = \mathcal{A} \left(\frac{1}{\zeta^3} - \frac{h}{\zeta^4} \right), \quad (4)$$

where $\mathcal{A} = A/6\pi$. Given the system under study, in the following we assume $h = 1\text{nm}$.

The global balance between viscous forces produced by hydrodynamic flow and the forces resulting from the interaction potential provides an additional relation which allows one to determine u_z :

$$u_z 2\pi \int_0^R dr r \int_r^R dr' \frac{6\eta r'}{\zeta(r')^3} = 2\pi \int_0^R dr r U'(\zeta). \quad (5)$$

Here we have no contribution of external force since we expect gravity effects to be negligible as compared to Van der Waals attraction at this scales.

In practice the dynamical equations were solved in normalized units. Defining the dimensionless repulsion strength $\bar{A} = \mathcal{A}/\tilde{\gamma}h^2$, dimensionless variables are the normalized width $\bar{\zeta} = \zeta/h$, radius $\bar{r} = r\bar{A}^{1/2}/h$ and time $\bar{t} = tB\tilde{\gamma}\bar{A}^2/h^3$. Rewriting the model equations in a dimensionless form, the only parameter explicitly appearing in the equation is the normalized viscosity

$$\bar{\eta} = \frac{B\eta}{h^2} = \frac{D\Omega^2 c_0}{k_B T h^2} \eta. \quad (6)$$

A large value of $\bar{\eta}$ indicates a strong influence of viscosity. Since $\bar{\eta} \sim h^{-2}$ in (6), viscosity effects are seen to be important when h is small.

The other relevant dimensionless quantities are the normalized system size

$$\bar{R} = \frac{\bar{A}^{1/2} R}{h}, \quad (7)$$

normalized supersaturation

$$\bar{\sigma} = \frac{k_B T h}{\bar{A} \tilde{\gamma} \Omega} \sigma, \quad (8)$$

and the normalized crystal velocity (growth rate)

$$\bar{u}_z = \frac{h^2}{\bar{A}^2 \tilde{\gamma} B} u_z. \quad (9)$$

Two sets of simulations with different dimensionless viscosities, $\bar{\eta} = 10^{-5}$ and $\bar{\eta} = 10^{-2}$, were performed. They respectively aim at modeling low solubility crystals such as Calcium Carbonate (CaCO_3), and highly soluble crystals like salts and sugars.

Table 1. Constants used in the simulations. Other parameters intervening in the scalings are assumed to be independent of the system considered. These are the temperature $T = 300\text{K}$, the interaction strength $\mathcal{A} = 10^{-21}\text{J}$ and the typical separation $h = 1\text{nm}$. Surface stiffnesses at the crystal water interface are assumed equal to surface tensions and are rough estimations due to lack of data and/or to large variability of it found in the literature. The last column indicates the solution viscosity at saturation.

Material	c_0	$\Omega [\text{\AA}^3]$	$D [10^{-9}\text{m}^2/\text{s}]$	$\tilde{\gamma} [\text{mJ}/\text{m}^2]$	$\eta [\text{mPas}]$
CaCO_3 ^a	10^{25}	59	0.8	100	1
NaClO_3 ^b	$6 \cdot 10^{27}$	69	0.3	10	7
Glucose ^c	$3 \cdot 10^{27}$	194	0.2	100	10
Sucrose ^d	$3.5 \cdot 10^{27}$	355	0.2	100	100

^a [27, 28, 29] Calcium carbonate is in general characterised by a wide range of solubility due to its strong dependency on carbon dioxide presence. The value in absence of CO_2 at 25° is [30] $c_0 = 0.013\text{g}/\text{L} \approx 10^{23}$. However this value can increase of about two orders of magnitude when CO_2 is present as is the case in natural environments as sea water [31]. We assume the latter.

^b [32, 33, 34, 35] Data for the diffusion coefficient at saturation was not found. We estimated this value by extrapolating at higher concentration from [36]. Similarly we extrapolated the data for the viscosity from [34].

^c [37, 38, 39] There is lack of data for surface tension of glucose-water interfaces. We assume $\tilde{\gamma} \approx 100\text{mJ}/\text{m}^2$ as suggested by some experiments on sucrose [40].

^d [37, 40, 41, 42]. Diffusion constant was assumed similar to the one of Glucose.

For the latter class, we focused on Sodium Chlorate (NaClO_3), which was used in our previous work [9], and Glucose.

The value of the dimensionless viscosity depends on the physical parameters as described by (6). The values we chose for the simulations are rough estimations. For instance Glucose actually lies in an intermediate regime between $\bar{\eta} = 10^{-2}$ and $\bar{\eta} = 10^{-1}$. Some exploratory simulations were also performed at viscosities higher than 10^{-1} . Larger viscosities could be encountered in other natural materials as more complex sugars. In the case of sucrose for instance, we have $\eta \approx 100\text{mPa}$ so that $\bar{\eta} > 1$ at saturation [41]. As a summary, the parameters used in the simulations are listed in table 1.

Finally, the value of the normalized repulsion strength \bar{A} is chosen following the same lines as in [19]. For simplicity we assume $A \approx 10^{-20}\text{J}$ [20] to be the same for all materials considered in the following. We then obtain $\bar{A} = \mathcal{A}/\tilde{\gamma}h^2 = A/6\pi\tilde{\gamma}h^2$. In any case, the qualitative behavior is not influenced by this parameter which never appears explicitly in the normalized equations, and only contributes to the spatial and temporal scales on which phenomena can be observed.

3. Discontinuous transition

We numerically solved (1) and (5) in a circular simulation box of fixed radius R , and fixed film width $\zeta(R) = \zeta_{bc}$ and supersaturation $\sigma(R) = \sigma_{bc}$ at the boundary of the integration domain. In all simulations we were able to reach a steady state characterized by a constant growth rate and crystal interface profile. We observe that for low enough viscosities $\bar{\eta}$, a cavity appears when increasing the simulation box radius R , or the boundary supersaturation σ_{bc} . In figure 1 we show two examples of simulations. The two columns were realized using different normalized viscosities $\bar{\eta}$,

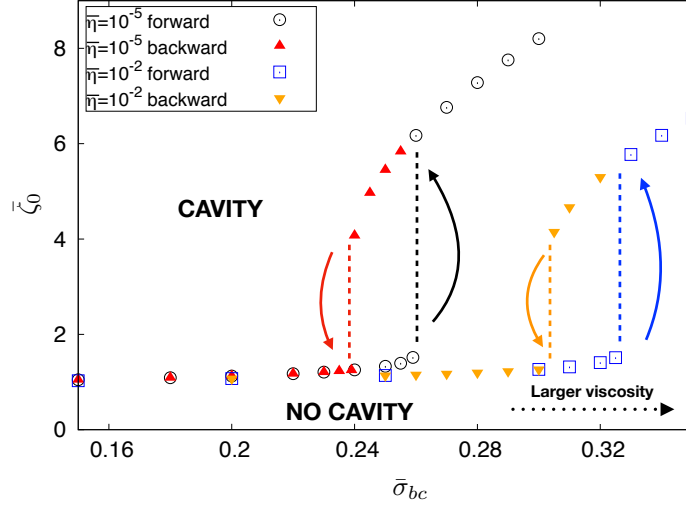


Figure 2. Film thickness at the center of the contact $\bar{\zeta}(r=0) = \bar{\zeta}_0$ versus supersaturation $\bar{\sigma}_{bc}$ at the boundary of the simulation box at different normalized viscosities $\bar{\eta}$. The size of the simulation box is $\bar{R} = 40$. The vertical axis is in nanometers. The size of the simulation box R and the supersaturation scale depend on the material. Calcium Carbonate, red triangles and black circles: $R = 400\text{nm}$, $\sigma_{bc} = 0.014 \times \bar{\sigma}_{bc}$; Sodium Chlorate, yellow triangles and blue squares: $R \approx 127\text{nm}$, $\sigma_{bc} = 0.017 \times \bar{\sigma}_{bc}$; Glucose, yellow triangles and blue squares: $R \approx 400\text{nm}$, $\sigma_{bc} = 0.05 \times \bar{\sigma}_{bc}$.

and keeping the other parameters fixed. Simulations at higher viscosity, e.g. $\bar{\eta} = 0.1$, do not show the appearance of a cavity.

For the two set of simulations considered, namely $\bar{\eta} = 10^{-2}$ and $\bar{\eta} = 10^{-5}$, we studied the steady state profiles close to the transition. In figure 2 we show as an example the variation of the normalized width $\bar{\zeta}(0) = \bar{\zeta}_0$ of the film in the center of the contact as a function of the normalized supersaturation $\bar{\sigma}_{bc}$, and for fixed box size $\bar{R} = 40$. Each dots corresponds to a steady state reached in a single simulation.

Considering a surface which is initially flat and in the minimum of the interaction potential ($\bar{\zeta}_0 = 1$), and gradually increasing the supersaturation $\bar{\sigma}_{bc}$, we observe a sharp jump in the value of $\bar{\zeta}_0$ at the transition. This process corresponds to black circles and blue squares in figure 2. However if we start with a system beyond the critical supersaturation, thus featuring a cavity, and slowly decrease the supersaturation $\bar{\sigma}_{bc}$, the transition is not observed at the same point, but at a lower supersaturation. This is represented by red and yellow triangles in figure 2. Hence, the transition exhibits hysteresis. A similar behavior is observed when looking at the crystal growth rate. This is showed in figure A1, where the discontinuity is less apparent especially in the backward transition (i.e. when decreasing the supersaturation).

No qualitative difference is observed between simulations at $\bar{\eta} = 10^{-2}$ and $\bar{\eta} = 10^{-5}$. The main difference lies in the shift of the transition towards larger supersaturations when the viscosity is increased.

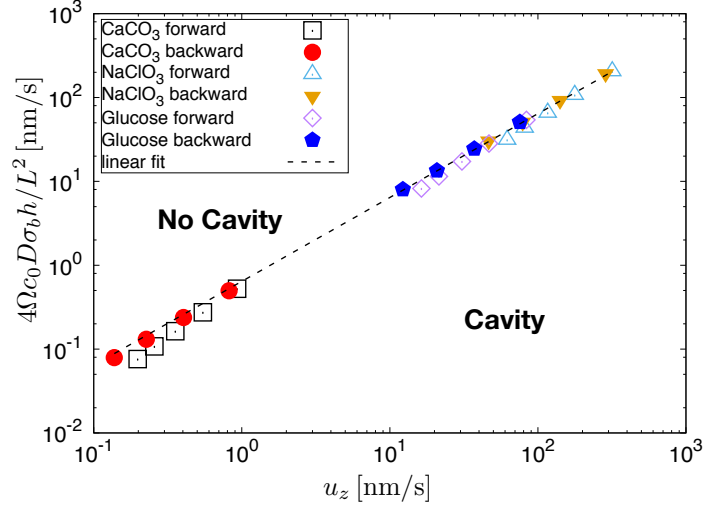


Figure 3. Non-equilibrium phase diagram for cavity formation for different materials and transition pathways. The scaled viscosity $\bar{\eta}$ is assumed to be 10^{-5} for CaCO_3 and 10^{-2} for NaClO_3 and Glucose.

4. Non-equilibrium morphology diagram

In [9], the conditions under which the formation of a cavity can be observed were summarized in a non-equilibrium morphology diagram. Let us recall the derivation of the condition for the transition following the same lines as in [9]. Consider steady state with a flat contact. From mass conservation (neglecting the consequences of solute advection), the total mass entering the liquid film from the boundary of a disc of radius r must be equal to the mass entering the crystal, leading to

$$\pi r^2 J_k = 2\pi r h J_d(r), \quad (10)$$

where h is the film thickness, J_k is the mass flux entering the crystal per unit area and $J_d(r)$ is the the diffusion flux entering the liquid film. Integrating the previous relation and using the identities $J_k = |u_z|/\Omega$ where $|u_z|$ is the growth rate, and $J_d(r) = D\partial_r c$, we obtain the concentration profile c . Then, using the definition of the supersaturation $\sigma = c(r)/c_0 - 1$, we find

$$\sigma(0) = \sigma_b - \frac{|u_z|}{4hDc_0\Omega} L^2, \quad (11)$$

where L and $\sigma_b = \sigma(L)$ are respectively the radius and the supersaturation at the boundary of the contact area. Using $\sigma(0) \leq 0$ as condition for cavity formation, we obtain the growth rate at the threshold

$$\alpha |u_z^{cav}| = 4D\Omega c_0 \sigma_b^{cav} \frac{h}{L^2}. \quad (12)$$

Following [9], the heuristic multiplicative constant α is introduced in order to capture quantitatively the simulation results within this simplified approach.

In order to build a non-equilibrium morphology diagram representing the location of the transition (when it exists) in a plane where the axes are the left hand side and

right hand side of (12), we need to evaluate the observables L and σ_b^{cav} . First, we determine the couple R and σ_{bc} at the transition. Then, we consider the contact radius L from the condition that $\zeta(L)$ exceeds the equilibrium position h by 1%. Finally we obtain σ_b^{cav} using

$$\sigma_b = \frac{\Delta\mu(L)}{k_B T} = \frac{\Omega}{k_B T} \left[\gamma \kappa(L) - U'(\zeta(L)) \right], \quad (13)$$

where κ is the local mean curvature. The procedure is repeated for simulations at different box sizes and viscosities, and on the different branches of the hysteresis curve.

The results, shown in figure 3, confirm the expected linearity of the transition line. Interestingly, the forward and the backward transitions roughly collapse on the same line. The differences in mass transport kinetics between different materials however lead to differences in the orders of magnitude of the critical vertical growth velocity u_z^{cav} (from about 0.1 to 100nm). A linear fit for the slope of the transition line leads to $\alpha = 0.65 \pm 0.04$. This result is close to the value $\alpha \approx 0.61$ obtained in [9]. However, the model of [9] was different, with a purely repulsive potential and a load to maintain the crystal close to the substrate. This result suggests that the constant α could be robust with respect to the details of the model.

5. Critical supersaturation and critical viscosity

To understand how viscosity can affect the transition we resort to a perturbative analysis of the steady-state solution. This is done assuming that, just before the transition, the profile deviates slightly from the equilibrium configuration $\zeta = \zeta_{eq} + \delta\zeta$. The details of the derivation, reported in Appendix B, reveal that the perturbation $\delta\zeta$ exhibits a concave parabolic profile. Hence, the thickness ζ_0 in the center of the contact increases as the supersaturation increases even in the absence of cavity.

This result suggests a simple mechanism for cavity formation. We use the standard result of the linear stability analysis of an infinite flat profile of thickness ζ , which indicates that the surface of the crystal should be stable when $U''(\zeta) > 0$, and unstable when $U''(\zeta) < 0$. This is similar to usual spinodal decomposition [43]. Hence, the initial profile with $\zeta = h$ is constant and at the minimum of the potential with $U''(h) > 0$ corresponds to a stable configuration. Considering now a non-equilibrium profile with a concave parabolic $\zeta(r)$, an approximate criterion for the cavity to form is that the thickness $\zeta_0 = \zeta(r = 0)$ at the center of the contact reaches the inflection point ζ^{cav} of the potential, with $U''(\zeta^{cav}) = 0$. This scenario is consistent with a discontinuous transition, since upon destabilization the thickness ζ_0 in the center of the contact becomes larger than ζ^{cav} . Once the instability is initiated, the larger ζ_0 , the larger $U''(\zeta_0)$, and the stronger the destabilization, leading to a self-amplifying feedback. Note once again that this behavior is reminiscent of spinodal instabilities [44, 45, 46].

Using this simple argument, i.e. $\zeta_0 = \zeta^{cav}$, and in the limit of large contacts, we find an expression for the critical supersaturation:

$$\sigma_b^{cav} \approx \frac{\mathcal{A}\Omega}{3k_B T h^3} \left(\frac{1 + 12\bar{\eta}}{1 - 12\bar{\eta}} \right). \quad (14)$$

The details of the derivation are reported in Appendix B.

As a first consequence of (14), the critical supersaturation σ_b^{cav} is expected to reach a finite value σ_b^* , when the viscosity vanishes. This result differs from

the behavior of purely repulsive potentials discussed in [9], where vanishingly small supersaturations were able to destabilize large crystals. This difference is intuitively understood from the fact that the supersaturation here needs to be large enough to lead to an escape of the crystal surface from the potential well at $\zeta = h$. Thus the thermodynamic force related to supersaturation $\Delta\mu/\Omega$ must be larger than the disjoining force dragging the interface towards the minimum of the potential $U'(\zeta^{cav}) \approx (\zeta^{cav} - h)U''(h)$. Since $\sigma_b = \Delta\mu_b/k_B T$, we obtain that $\sigma_b^* = (\zeta^{cav} - h)U''(h)/(\Omega k_B T)$, which is identical to (14) when $\bar{\eta} = 0$ and U is given by (3). This result, which states that the critical supersaturation σ_b^{cav} is expected to reach a constant value when the viscosity vanishes and the size is large, is confirmed by simulations in figure 4 for small viscosities (blue and red triangles). However, the predicted value $\bar{\sigma}_b^* \approx 0.33$ is larger than the value observed in simulations $\bar{\sigma}_b^{cav}(L \rightarrow \infty) \approx 0.12$. Going back to physical variables $\sigma = \bar{\sigma}\mathcal{A}\Omega/(k_B T h^3)$, we find that the critical supersaturation at vanishing viscosities is small $\sigma_b^* \sim 10^{-2}$ to 10^{-3} for $h \sim 1\text{nm}$. Since $\sigma_b^* \sim h^{-3}$, the critical supersaturation decreases quickly when the equilibrium thickness h increases, and $\sigma_b^* < 10^{-5}$ for $h = 10\text{nm}$.

The expression (14) also provides information about the consequences of viscosity. For example, it agrees qualitatively with figure 2, where higher viscosities were shown to lead to a transition at higher supersaturations. In figure 4, we show the normalized critical (forward) supersaturation $\bar{\sigma}_b^{cav}$ at different normalized viscosities as obtained by simulations. This again confirms good qualitative agreement with (14), since it agrees both with the increase of σ_b^{cav} with increasing $\bar{\eta}$, and with the divergence of σ_b^{cav} for a finite value of $\bar{\eta}$.

However, (14) is quantitatively inaccurate. For example, the observed threshold at $\bar{\eta}^* \approx 0.034$ is lower than the predicted value $\bar{\eta}^* = 1/12 \approx 0.08$. Despite the absence of a quantitatively accurate expression for the critical supersaturation as a function of viscosity, it is possible to obtain quantitative insights about the critical viscosity using the morphology diagram. Indeed, inserting the parabolic profile $\zeta_{eq} + \delta\zeta$ of the film in the contact in the force balance equation (5), leads to a second relation valid below the transition

$$u_z \approx \frac{-4hD\Omega c_0 \sigma_b}{(6\bar{\eta} + 1/2)L^2}. \quad (15)$$

The details of this derivation are presented in Appendix B.2. This expression exhibits quantitative agreement with simulation results as illustrated in figure B2. It follows from (15) that, as viscosity increases, the growth rate u_z decreases. In addition, for low viscosities the growth rate is independent of the viscosity.

Inserting (15) in (12), we find the critical value of the viscosity above which the cavity cannot form

$$\frac{D\Omega^2 c_0}{k_B T h^2} \bar{\eta}^* = \bar{\eta}^* = \frac{2\alpha - 1}{12} \approx 0.025 \pm 0.007. \quad (16)$$

Interestingly, if we assume the idealized case to hold ($\alpha = 1$), we would have obtained $\bar{\eta}^* = 1/12$ as in (14). Even though (15) and (16) rely on some approximations—based on our perturbative analysis and on the heuristic character of the parameter α —we find that (16) provides a reasonably accurate prediction close to the value $\bar{\eta}^* \approx 0.034$ from the full numerical solution of the model.

The discussion of this result can be presented in two different ways. First, we may assume that disjoining pressure effects lead to a fixed film thickness, assumed

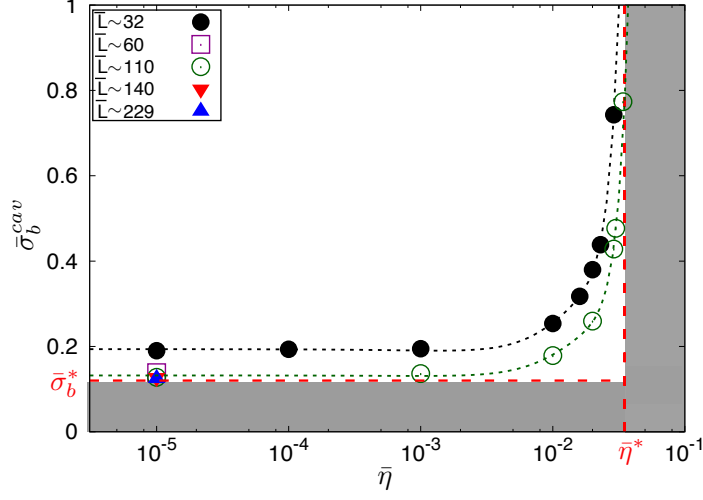


Figure 4. Critical supersaturation for the appearance of a cavity as a function of viscosity, as obtained from simulations for the forward transition (initially flat contact). The results are reported in normalized units. The critical supersaturation diverges at $\bar{\eta}^* \approx 0.34$. For larger normalized viscosities, cavities are not observed in simulations independently from the size of the contact (shaded area). The critical supersaturation converges to a fixed value when the contact size increase at fixed viscosity, as predicted by (B.16) and (14). At vanishing viscosity the critical supersaturation is $\bar{\sigma}_b^* \approx 0.12$ (red and blue triangles). Cavities cannot be observed independently from the size of the contact below this value (shaded area).

for example to be $h \approx 1$ nm. Then, using (16) and considering the materials listed in table 1, we find $\eta^* \approx 3.7 \times 10^3$ mPas for Calcite, $\eta^* \approx 12$ mPas for Sodium Chlorate, $\eta^* \approx 4.6$ mPas for Glucose and $\eta^* \approx 1.2$ mPas for Sucrose. Cavity formation should be hindered or suppressed by viscosity effects when these values are equal to, or smaller than the values of viscosity at saturation reported in the last column of table 1. These are 1, 7, 10 and 100 mPas, respectively. Thus, for example we do not expect a cavity to appear for Sucrose while Calcite could feature a cavity. Conclusions on Glucose or Sodium Chlorate are more difficult since the value of the critical viscosity is close to the viscosity at saturation.

The threshold can be reformulated in a different manner. Indeed, since the value of the critical viscosity increases as the square of h there is a critical thickness h^* above which a cavity can form for a given system. Using the viscosity at saturation, we find $h^* \approx 0.016$ nm for CaCO_3 , $h^* \approx 0.76$ nm for NaClO_3 , $h^* \approx 1.5$ nm for Glucose, and $h^* \approx 9.2$ nm for Sucrose. These results once again state that cavity formation should be suppressed for Sucrose with nanoscale confinement. For other materials with smaller viscosities, the main effect of viscosity should be to shift the transition as shown in figure 2 and figure 3. In general, when the film thickness is larger than $h \approx 10$ nm as in [9, 12], we expect cavities can form for most materials.

6. Discussion

Some limitations of our approach are discussed in this section. The first one concerns the difficulty to analyze strongly anisotropic crystals which exhibit facets. Indeed, the stiffness $\tilde{\gamma}$ is expected to diverge at faceted orientations. However, in [9], satisfactory quantitative agreement with experimental data for faceted crystals was obtained using a large but finite stiffness. Applying this *ad hoc* assumption to the results of the present paper would not change them qualitatively. However, the value of some physical observables would change. If we assume an effective stiffness about 10^3 - 10^4 times the surface tension [9], crystal velocities (see figure 3) reduce by the same factor. In addition, due to our stiffness-dependent normalization of space variables, our simulations would correspond to larger crystal sizes (by a factor 10 - 100). In any case this will not change the measured slope α of the non-equilibrium phase diagram nor the value of the critical viscosity since these quantities are independent of the stiffness.

A second difficulty is to use continuum models to describe the consequences of nano-scale confinement on diffusion and hydrodynamics. It is known for example that diffusion constants in water can vary significantly with confinement [47]. In contrast, the hydrodynamic description of water with bulk viscosity is known to be quantitatively accurate for separations larger than ~ 1 nm [47]. At the nanoscale, liquids can also be structured in the vicinity of solid surfaces. For example, layering may lead to oscillations in the disjoining pressure [20]. Additional confinement effects specific to solutions appear when the liquid film thickness is decreased up to values that are comparable to the size of the solute molecules. Such confinement effects could be observed, e.g., for sucrose which exhibits a molecular size of the order of one nanometer. Globally, using continuum models to probe nanoscale hydrodynamic effects is a challenge. In order to reach quantitative accuracy, such methods must be based on effective models which are calibrated on molecular simulations to account for possible deviations from the bulk behavior. This strategy should allow one to describe some of the consequences of confinement by means of the thickness-dependence of physical parameters such as the diffusion constant and the viscosity. Achieving this goal would be an important step toward the modeling of crystal growth with nanoscale confinement. Indeed, modeling of the growth process in standard molecular dynamics simulations is difficult due to prohibitive computational time.

Another phenomenon which comes to the fore at the nanoscale is thermal fluctuations. While the model discussed here is purely deterministic, atomistic simulations such as Molecular Dynamics or Monte Carlo Simulations [48] can account for fluctuations. Thermal fluctuations could trigger the random opening and closure of the cavity observed in NaClO_3 crystals reported in Ref. [9]. Larger-scale fluctuations or perturbations, such as those due to convection or stirring in the bulk fluid outside the crystal, should not be relevant here, since they influence mass transport at scales larger than the thickness of the diffusion boundary layer $\ell_{BL} = D/u_L$ at the free surface of the crystal, which is itself larger than the film thicknesses h considered here. Indeed, taking $D \sim 10^{-9} \text{m}^2/\text{s}$, we would need a very large hydrodynamic velocity $u_L \sim 10 \text{cm/s}$ outside the contact region for ℓ_{BL} to reach a scale comparable to that of the liquid film in the contact $h \sim 10 \text{nm}$.

As already mentioned in the introduction, since it leads to growth perpendicular to the substrate incorporation of mass in the crystal at contacts may lead to the generation of forces on the substrate [14, 15, 8, 16]. These crystallization forces play

an important role in geology since they are responsible for deformation and fracturing of rocks, and are also crucial for the weathering of building materials [17, 18]. Even though these forces are well characterized at equilibrium via energy balance [49, 50], we still lack a precise understanding of the related non-equilibrium dynamics. A major issue is for instance to understand the interplay between the force of crystallization and the non-equilibrium morphology of the contact [10], often characterized by the presence of a rim along the edge of the contact region [10, 11, 12, 13]. Despite the absence of external forces in our model, we hope that our results will provide hints toward a better understanding of the conditions under which rims can form.

7. Conclusions

In conclusion, we have studied the formation of cavities in nano-confined crystal surfaces. Examples are discussed for some model materials ranging from poorly soluble minerals (Calcite) to high soluble salts (Sodium Chlorate) and sugars.

Cavity formation was recently observed experimentally using NaClO_3 crystals with liquid film thicknesses that were one or two orders of magnitude larger than those used here [9]. Despite the different scales the resulting non-equilibrium morphology diagrams are very similar (with a similar value of the phenomenological constant α). This further confirms the robustness of cavity formation with respect to variations of physical conditions and materials.

However, some differences are observed at the nanoscale. First, we show that an attractive Van der Waals interaction induces a discontinuous (subcritical) transition with hysteresis. Moreover, there is a minimum supersaturation below which cavities cannot form because the driving force is not sufficient for the interface to escape from the potential well of the disjoining pressure (however its quantitative value is relatively small when h is larger than 1nm). Second, due to the nanoscale width of the liquid film separating the crystal and the confining wall, viscosity becomes relevant. The effect of viscosity is to shift the transition toward larger crystal sizes and larger supersaturations. Moreover, the formation of the cavity can also be prevented by sufficiently large viscosities. We estimated the relevant critical viscosity above which no cavity should appear. In practice, such condition could be realized for instance for sucrose.

We hope that our work will inspire novel experimental investigations or molecular simulations of growth after heterogeneous nucleation and of growth of sedimented crystals.

Acknowledgments

The authors wish to acknowledge funding from the European Union's Horizon 2020 research and innovation program under grant agreement No 642976.

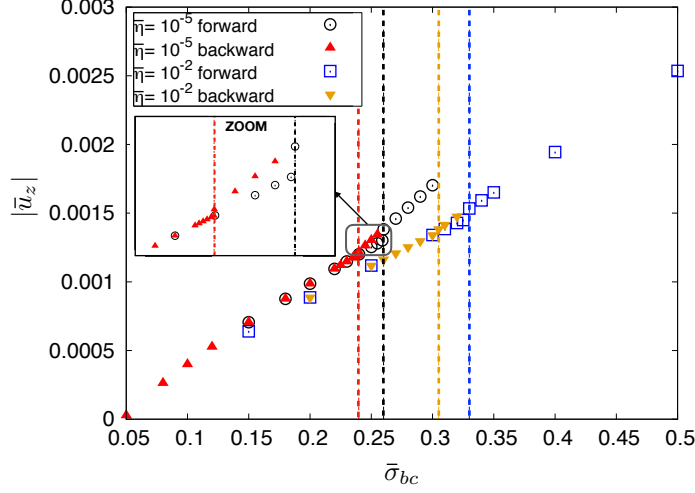


Figure A1. Normalized growth rate $|\bar{u}_z|$ versus supersaturation $\bar{\sigma}_{bc}$ at the boundary of the simulation box for different normalized viscosities $\bar{\eta}$. The size of the simulation box is $\bar{R} = 40$. The system size and scales of the axes depend on the material. Calcium Carbonate, red triangles and black circles: $R = 400\text{nm}$, $\sigma_{bc} \approx 0.014 \times \bar{\sigma}_{bc}$, $u_z \approx 6.7 \times 10\text{nm/s} \times \bar{u}_z$; Sodium Chlorate, yellow triangles and blue squares: $R \approx 127\text{nm}$, $\sigma_{bc} \approx 0.017 \times \bar{\sigma}_{bc}$, $u_z \approx 2.1 \times 10^5\text{nm/s} \times \bar{u}_z$; Glucose, yellow triangles and blue squares: $R \approx 400\text{nm}$, $\sigma_{bc} \approx 0.05 \cdot \bar{\sigma}_{bc}$, $u_z \approx 5.5 \times 10^4\text{nm/s} \times \bar{u}_z$. Vertical dashed lines indicate the critical supersaturation at the boundary of the simulation box for forward and backward transitions. Their color is the same as that of the corresponding symbols.

Appendix A. Growth rate as a function of supersaturation

In figure A1 we show the normalized growth rate \bar{u}_z as a function of the normalized supersaturation at the boundary of the simulation box as obtained from numerical solution of (1) and (5). The growth rate responds roughly linearly to changes in the supersaturation, and a small jump followed by a change of slope is observed at the transition. Hysteresis is also found here but the discontinuity is more apparent when increasing the supersaturation from an initial flat surface (forward transition).

Appendix B. Perturbation to equilibrium

Using a perturbative approach from the equilibrium solution of (1) and (5), we here derive approximate expressions for the growth rate and the critical supersaturation.

As a preamble, we characterize the equilibrium solution itself. Steady-state solution of (1) and (5) obey

$$0 = B \frac{1}{r} \partial_r [r \zeta \partial_r (\tilde{\gamma} \partial_{rr} \zeta + \frac{\tilde{\gamma}}{r} \partial_r \zeta - U'(\zeta))] + u_z. \quad (\text{B.1})$$

The equilibrium solution is a particular steady-state equation obeying $u_z = 0$ and

$$\tilde{\gamma} \partial_{rr} \zeta_{eq} + \frac{\tilde{\gamma}}{r} \partial_r \zeta_{eq} - U'(\zeta_{eq}) = \frac{\Delta \mu_{eq}}{\Omega}, \quad (\text{B.2})$$

where $\Delta\mu_{eq}/\Omega$ is a constant which corresponds to the equilibrium chemical potential. The radius of the contact region is denoted as L . Multiplying (B.2) by $2\pi r$, and integrating between the center of the contact at $r = 0$ and a radius $r = R > L$, we find a relation between the equilibrium chemical potential and the slope at the boundary of the integration domain

$$\frac{\Delta\mu_{eq}}{\Omega} = \frac{2\tilde{\gamma}}{R} \partial_r \zeta_{eq}(R), \quad (\text{B.3})$$

where we have used the relation $2\pi \int_0^R r dr U'(\zeta) = 0$, corresponding to the equilibrium force balance (5). A second relation can be found when multiplying (B.2) by $\partial_r \zeta_{eq}$ and integrating with respect to r :

$$\frac{\tilde{\gamma}}{2} (\partial_r \zeta_{eq}(R))^2 - \Delta U = \frac{\Delta\mu_{eq}}{\Omega} (\zeta_{eq}(R) - \zeta_{eq}(0)) - \tilde{\gamma} \int_0^R \frac{(\partial_r \zeta)^2}{r} dr, \quad (\text{B.4})$$

where $\Delta U = U(\zeta_{eq}(R)) - U(\zeta_{eq}(0))$. Equation (B.4) relating the surface slope $\partial_r \zeta_{eq}(R)$ outside the contact to the depth of the potential well ΔU , is equivalent to a generalized form of the Young contact angle condition. The integral term in the second equation is related to the effect of line tension. In the following, we will neglect this term.

We now assume that the equilibrium profile is flat $\zeta_{eq}(r) \approx h$ with $U'(h) = 0$ for $r \leq L$. Then, we expect $\zeta_{eq}(L) \approx \zeta_{eq}(0) \approx h$, and combining (B.4) and (B.3) we find

$$\Delta\mu_{eq} \approx \frac{2\Omega}{L} \sqrt{-2\tilde{\gamma}U(h)}, \quad (\text{B.5})$$

where we assumed that the interaction potential vanishes far from the contact region $U(\zeta(r > L)) \approx 0$. Note that under these approximations the right hand side of (B.4) vanishes, and this equation is the small slope limit of the Young contact angle condition.

Consider now a system below the transition, so that no cavity is present. The crystal surface profile is then expected to be close to the equilibrium profile. We therefore consider the difference $\delta\zeta(r) = \zeta(r) - \zeta_{eq}(r)$ between the steady-state solution and the equilibrium solution to be small. Expanding (B.1) to linear order in $\delta\zeta(r)$, and integrating two times, we find

$$\tilde{\gamma} \partial_{rr} \delta\zeta + \frac{\tilde{\gamma}}{r} \partial_r \delta\zeta - \delta\zeta U''(\zeta_{eq}) - \frac{u_z}{2B} \int_r^L \frac{r'}{\zeta_{eq}(r')} dr' = \frac{\Delta\mu_b - \Delta\mu_{eq}}{\Omega}, \quad (\text{B.6})$$

where we have used the parity of $\zeta(r)$ and (B.2), and we have defined the chemical potential at the edge of the contact zone $\Delta\mu_b = \Delta\mu(L)$ with $\Delta\mu(L)$ given by (2). Assuming again that in the contact area $r < L$ the equilibrium profile is flat $\zeta_{eq} \approx h$, (B.6) can be rewritten as:

$$\tilde{\gamma} \partial_{rr} \delta\zeta + \frac{\tilde{\gamma}}{r} \partial_r \delta\zeta - \delta\zeta U''(h) - \frac{u_z}{4Bh} (L^2 - r^2) = \frac{\Delta\mu_b - \Delta\mu_{eq}}{\Omega}. \quad (\text{B.7})$$

A particular solution of this equation is a parabola:

$$\delta\zeta = \frac{u_z}{4BhU''(h)} (r^2 - L^2) + \frac{4\tilde{\gamma}}{U''(h)} - \frac{\Delta\mu_b - \Delta\mu_{eq}}{\Omega U''(h)}. \quad (\text{B.8})$$

A comparison between this solution and the profile obtained from numerical integration is shown in figure B1 for crystal close to the transition. The agreement is very satisfactory.

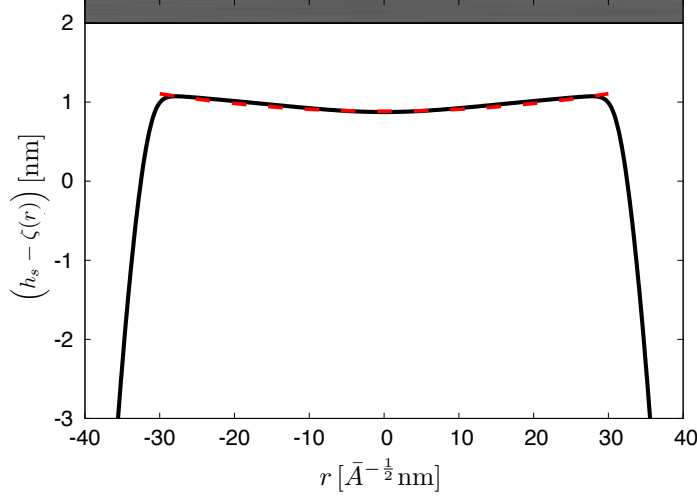


Figure B1. Section of the crystal profile close to the transition. The black zone at the top represents the substrate. The black line is the simulation result. The vertical axis is in physical units. The horizontal axis scaling depends on the material (via the constant \bar{A}). Simulation parameters: size of the box $\bar{R} = 40$, supersaturation at the boundary of the integration domain $\bar{\sigma}_{bc} = 0.2$. The dashed red line is obtained from (B.8) with L , u_z , $\Delta\mu_b$ measured in the simulation.

Appendix B.1. Viscosity effect on the growth rate

Applying a similar procedure to the force balance expression in (5) we have to leading order

$$u_z 2\pi \int_0^L dr r \int_r^L dr' \frac{6\eta r'}{\zeta_{eq}^3(r')} = 2\pi \int_0^L dr r \delta\zeta U''(\zeta_{eq}). \quad (\text{B.9})$$

Using (B.6) to express the right hand side, we are left with

$$\begin{aligned} u_z 2\pi \int_0^L dr r \int_r^L dr' r' \left(\frac{6\eta}{\zeta_{eq}^3(r')} + \frac{1}{2B\zeta_{eq}(r')} \right) = \\ = -\pi L^2 \frac{\Delta\mu_b - \Delta\mu_{eq}}{\Omega} + 2\pi\tilde{\gamma} L \partial_r \delta\zeta(L). \end{aligned} \quad (\text{B.10})$$

As done previously we assume that in the contact area $r < L$, the equilibrium profile is $\zeta_{eq} \approx h$. With this assumption the previous relation reduces to

$$u_z \left(\frac{6\eta}{h^3} + \frac{1}{2Bh} \right) \frac{L^4}{4} = -L^2 \frac{\Delta\mu_b - \Delta\mu_{eq}}{\Omega} + 2L\tilde{\gamma} \partial_r \delta\zeta(L). \quad (\text{B.11})$$

Using (B.8) to express the last term in the right hand side we have

$$\frac{L^4}{4} \left[\left(\frac{6\eta}{h^3} + \frac{1}{2Bh} \right) - \frac{4\tilde{\gamma}}{L^2 B h U''(h)} \right] u_z = -L^2 \frac{\Delta\mu_b - \Delta\mu_{eq}}{\Omega}. \quad (\text{B.12})$$

We then obtain

$$u_z = \frac{-4Bh(\Delta\mu_b - \Delta\mu_{eq})}{\left(\frac{6B}{h^2}\eta + \frac{1}{2} - \frac{4\tilde{\gamma}}{L^2 U''(h)} \right) L^2 \Omega}. \quad (\text{B.13})$$

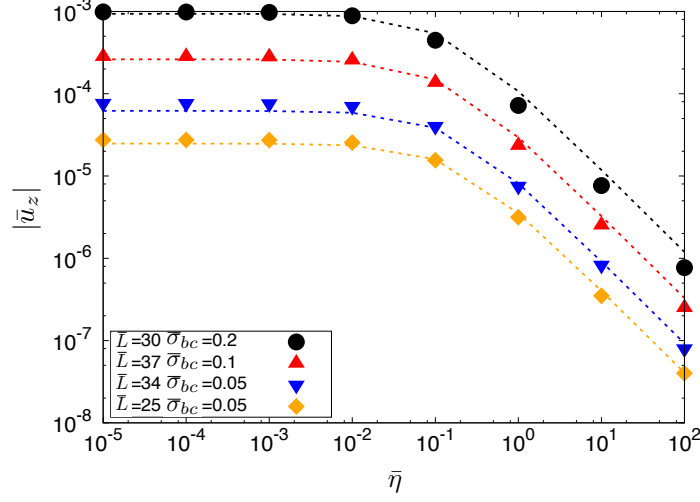


Figure B2. Growth rate $|u_z|$ as a function of the viscosity shown in normalized units before undergoing the transition (flat growth) for different sizes. The dots are simulation results, the dashed lines were computed using (B.13) with L and $\Delta\mu_b(\eta)$ (see (13)) measured in simulations and $\Delta\mu_{eq}$ given by (B.5). The value of the contact size L varies weakly when the viscosity is varied.

As showed in figure B2 the comparison between this relation and the direct numerical solution of u_z proves to be satisfactory.

Here, we wish to focus on steady-states close to the threshold of cavity formation. Since $\Delta\mu_{eq} \sim 1/L$ from B.5, this term can be neglected far from equilibrium and for large system sizes where cavity formation occurs. For the same reason we neglect the term of order $1/L^2$. Finally, assuming the supersaturation is small, we have $\Delta\mu_b = k_B T \sigma_b$, and we obtain (15).

Appendix B.2. Viscosity effect on the critical supersaturation

As discussed in the main text, we expect the cavity to appear when $\zeta_0 > \zeta^{cav}$, where ζ_0 is the width at the center of the contact, and ζ^{cav} is defined by the relation $U''(\zeta^{cav}) = 0$. Given (4) and assuming again $\zeta_{eq} \approx h$, we find $\zeta^{cav} = 4/3 h$ and $\delta\zeta^{cav} = \zeta^{cav} - h = h/3$. Let us recall (B.8) and consider the correction to ζ_0 :

$$\delta\zeta(0) = \frac{u_z}{4BhU''(h)} \left(\frac{4\tilde{\gamma}}{U''(h)} - L^2 \right) - \frac{\Delta\mu_b - \Delta\mu_{eq}}{\Omega U''(h)}. \quad (\text{B.14})$$

Now we use the condition $\delta\zeta(0) = \delta\zeta^{cav}$ for the appearance of the cavity, and deduce the corresponding critical value of the chemical potential at the boundary:

$$\frac{\Delta\mu_b^{cav} - \Delta\mu_{eq}}{\Omega} = \frac{u_z}{4Bh} \left(\frac{4\tilde{\gamma}}{U''(h)} - L^2 \right) - \delta\zeta^{cav} U''(h). \quad (\text{B.15})$$

Using (B.13) we have

$$\frac{\Delta\mu_b^{cav} - \Delta\mu_{eq}}{\Omega} \approx \frac{\delta\zeta^{cav} U''(h) \left(\frac{6B}{h^2} \eta + \frac{1}{2} - \frac{4\tilde{\gamma}}{L^2 U''(h)} \right)}{\frac{1}{2} - \frac{6B}{h^2} \eta}. \quad (\text{B.16})$$

Using again the identity $\Delta\mu = k_B T \sigma$, neglecting the last term in the denominator ($\sim 1/L^2$) and the equilibrium chemical potential ($\sim 1/L$), we obtain (14).

References

- [1] Markov I V 2017 *Crystal Growth for Beginners* 3rd ed (World Scientific, Singapore) ISBN 9813143428
- [2] Turnbull D 1950 *The Journal of Chemical Physics* **18** 198–203 ISSN 00219606
- [3] Winter D, Virnau P and Binder K 2009 *Physical Review Letters* **103** 1–4 ISSN 00319007 (Preprint 1001.3336)
- [4] Page A J and Sear R P 2006 *Physical Review Letters* **97** 1–4 ISSN 00319007
- [5] Chayen N E, Saridakis E and Sear R P 2006 *Proceedings of the National Academy of Sciences of the United States of America* **103** 597–601 ISSN 0027-8424
- [6] Durney D W 1972 *Nature* **253** 315–317 ISSN 00280836
- [7] Weyl P K 1959 *Journal of Geophysical Research* **64** 2001–2025 ISSN 2156-2202
- [8] Desarnaud J, Bonn D and Shahidzadeh N 2016 *Scientific Reports* **6** 30856 ISSN 2045-2322
- [9] Kohler F, Gagliardi L, Pierre-Louis O and Dysthe D K 2018 *Submitted* (Preprint 1802.00310)
- [10] Robert J Flatt, Michael Steiger G W S 2007 *Environ Geol* **52** 187–203
- [11] Røyne A and Dysthe D K 2012 *Journal of Crystal Growth* **346** 89–100 ISSN 0022-0248
- [12] Li L, Kohler F, Røyne A and Dysthe D 2017 *Crystals* **7** 361 ISSN 2073-4352
- [13] Taber S 1916 *American Journal of Science* 532–556
- [14] Becker G F and Day A L 1916 *The Journal of Geology* **24** 313–333
- [15] Correns C W and Steinborn W 1939 *Zeitschrift für Kristallographie-Crystalline Materials* **101** 117–133
- [16] Naillon A, Joseph P and Prat M 2018 *Physical Review Letters* **120** 34502 ISSN 1079-7114
- [17] Flatt R J 2002 *Journal of Crystal Growth* **242** 435–454 ISSN 00220248
- [18] Espinosa-Marzal R M and Scherer G W 2010 *Accounts of chemical research* **43** 897–905
- [19] Gagliardi L and Pierre-Louis O 2018 *Physical Review E* **97** 012802 ISSN 2470-0045
- [20] Israelachvili J N 1991 *Intermolecular and Surface Forces Third Edition* 3rd ed (Academic Press) ISBN 0123751829
- [21] Verwey E J W and Overbeek J T G 1948 *Theory of the stability of lyophobic colloids* (Elsevier Publishing Company. INC.) ISBN 00223654 (ISSN)
- [22] Alcantar N, Israelachvili J and Boles J 2003 *Geochimica et Cosmochimica Acta* **67** 1289–1304 ISSN 00167037
- [23] Valle-Delgado J J, Molina-Bolívar J A, Galisteo-González F, Gálvez-Ruiz M J, Feiler A and Rutland M W 2005 *Journal of Chemical Physics* **123** 1–12 ISSN 00219606
- [24] Hamilton A, Koutsos V and Hall C 2010 *Chemical Communications* **46** 5235 ISSN 1359-7345
- [25] Diao Y and Espinosa-marzal R M 2016 *PNAS* **113** 12047–12052
- [26] Oron A and Bankoff S G 1997 *Reviews of Modern Physics* **69** 931–980 ISSN 0034-6861
- [27] Yuan-Hui L and Gregory S 1974 *Geochimica et Cosmochimica Acta* **38** 703–714 ISSN 00167037
- [28] Røyne A, Bisschop J and Dysthe D K 2011 *J. Geophys. Res.* **116** B04204 ISSN 0148-0227
- [29] 2017 National Center for Biotechnology Information. PubChem Compound Database; CID=10112
- [30] Tegethoff F W (ed) 2001 *Calcium Carbonate* (Basel: Birkhäuser Basel) ISBN 978-3-0348-9490-6
- [31] Miller J P 1952 *American Journal of Science* **250** 161–203
- [32] Seidell A 1919 *Solubilities of inorganic and organic substances* (New York, Van Nostrand)
- [33] Misbah C, Renard F, Gratier J P and Klaus K 2004 *Geophysical Research Letters* **31** 1–5 ISSN 0094-8276
- [34] Campbell A, Kartzmark E and Olivier B G 1966 *Canadian Journal of Chemistry* **44** 925–934
- [35] Lide D R (ed) 2005 *Handbook of Chemistry and Physics* 86th ed (CRC Press (Taylor and Francis Group)) ISBN 0-8493-0486-5
- [36] Campbell A and Oliver B 1969 *Canadian Journal of Chemistry* **47** 2681–2685 ISSN 1480-3291
- [37] Gladden J K and Dole M 1953 *Journal of the American Chemical Society* **75** 3900–3904 ISSN 15205126
- [38] Viet Bui A and Nguyen M H 2004 *Journal of Food Engineering* **62** 345–349 ISSN 02608774
- [39] 2017 National Center for Biotechnology Information. PubChem Compound Database; CID=5793
- [40] Honig P 1959 *Principles of Sugar Technology, Volume II Crystallisation* elsevier p ed
- [41] Mathlouthi M and Reiser P 1995 *Sucrose* springer s ed vol 69 ISBN 0751402230
- [42] 2017 National Center for Biotechnology Information. PubChem Compound Database; CID=5988
- [43] Cahn J W 1961 *Acta Metallurgica* **9** 795–801 ISSN 00016160

- [44] Mitlin V S and Petviashvili N V 1994 *Physics Letters A* **192** 323–326 ISSN 03759601
- [45] Herminghous S, Jacobs K, Mecke K, Bischof J, Fery A, Ibn-Elhaj M and Schlagowski S 1998 *Science* **282** 916
- [46] Xie R, Karim A, Douglas J F, Han C C and Weiss R A 1998 *Physical Review Letters* **81** 1251–1254 ISSN 10797114
- [47] Bocquet L and Charlaix E 2010 *Chem. Soc. Rev.* **39** 1073–1095 ISSN 0306-0012
- [48] Høgberget J, Røyne A, Dysthe D K and Jetttestuen E 2016 *Physical Review E - Statistical, Nonlinear, and Soft Matter Physics* **94** 1–12
- [49] Steiger M 2005 *Journal of Crystal Growth* **282** 470–481 ISSN 00220248
- [50] Steiger M 2005 *Journal of Crystal Growth* **282** 455–469 ISSN 00220248